

Correlated 3D Nanoscale Mapping and Simulation of Coupled Plasmonic Nanoparticles

Georg Haberfehlner,^{*†,‡} Andreas Trügler,[§] Franz P. Schmidt,[‡] Anton Hörl,[§] Ferdinand Hofer,^{†,‡} Ulrich Hohenester,[§] and Gerald Kothleitner^{†,‡}

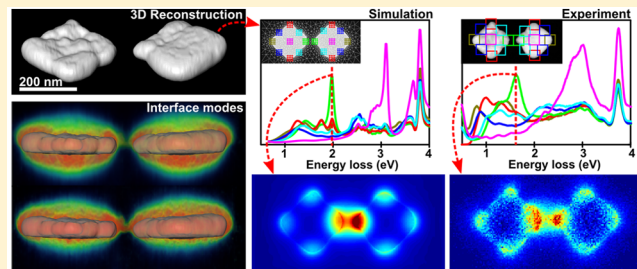
[†]Graz Centre for Electron Microscopy, Steyrergasse 17, 8010 Graz, Austria

[‡]Institute for Electron Microscopy and Nanoanalysis, Graz University of Technology, Steyrergasse 17, 8010 Graz, Austria

[§]Institute of Physics, University of Graz, Universitätsplatz 5, 8010 Graz, Austria

S Supporting Information

ABSTRACT: Electron tomography in combination with electron energy-loss spectroscopy (EELS) experiments and simulations was used to unravel the interplay between structure and plasmonic properties of a silver nanocuboid dimer. The precise 3D geometry of the particles fabricated by means of electron beam lithography was reconstructed through electron tomography, and the full three-dimensional information was used as an input for simulations of energy-loss spectra and plasmon resonance maps. Excellent agreement between experiment and theory was found throughout, bringing the comparison between EELS imaging and simulations to a quantitative and correlative level. In addition, interface mode patterns, normally masked by the projection nature of a transmission microscopy investigation, could be unambiguously identified through tomographic reconstruction. This work overcomes the need for geometrical assumptions or symmetry restrictions of the sample in simulations and paves the way for detailed investigations of realistic and complex plasmonic nanostructures.



KEYWORDS: Plasmonics, nanoparticles, electron tomography, electron energy loss spectroscopy, electron beam lithography

Plasmonics confines light to subdiffraction volumes through excitation of collective electron charge oscillations at the boundaries of metallic nanoparticles, so-called surface plasmons,^{1,2} and holds promise for various applications in photonics, optoelectronics, and (bio)sensing.^{2,3} By tailoring shape and alignment of metallic nanoparticles, it becomes possible to control properties of localized surface plasmon resonances (LSPRs), such as spectral peak positions or near-field couplings and enhancements.^{1,2,4–6} In particular the top-down approach of electron beam lithography plays an important role in the quest of versatile nanoparticle manufacturing,^{7–11} but the technique usually suffers from imperfections, surface roughness, and limited spatial resolution, which leads to nanoparticle shapes that deviate from the design objectives. Similar limitations apply to chemical synthesis, which generally leads to metallic nanoparticle ensembles with size dispersion and nonidentical geometries. Therefore, to exploit the full potential of plasmonics, full 3D characterization and simulation tools taking into account the imperfections of real structures become mandatory.

Monochromated EELS together with scanning transmission electron microscopy (STEM) provides a powerful combination to investigate individual plasmonic nanoparticles with high spatial (subnanometer) and energy (sub 100 meV) resolution.^{12–14} Experimental data sets from which both the spatial

2D and energetic information can be retrieved, termed spectrum images (SI), have been used intensively to investigate LSPRs in various nanostructures.^{5–11,15–18} The major limitation of this approach is the two-dimensional character of the technique, preventing the plasmon modes and the corresponding electromagnetic fields to be resolved in full 3D, since the spatial field distribution in the direction of the electron beam cannot be recovered from a single SI.

Although spectroscopic electron tomography is nowadays successfully and routinely employed in material science applications,^{19–26} tomographic EELS mapping of LSPRs is complicated by the nonlocal self-interaction character of the plasmonic energy loss, where the swift electron first excites a LSPR and then performs work against the induced plasmon field.^{27,28} Tomographic plasmon field reconstruction is generally possible only under restrictive assumptions, such as the applicability of the quasistatic approximation or a plasmonic response governed by a single mode, and was demonstrated in a single proof-of-principle experiment for a silver nanocube.²⁸ Possible routes to overcome these restrictions are based on inverse-problem schemes²⁹ or combined STEM and cathodo-

Received: September 18, 2015

Revised: October 22, 2015

Published: October 23, 2015



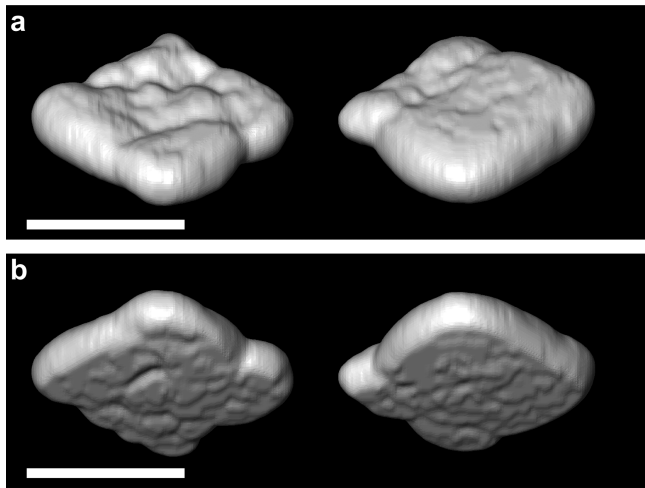


Figure 1. 3D reconstruction of the silver nanocuboids seen (a) from the top side and (b) from the bottom (substrate) side. Scale bars are 200 nm.

luminescence tomography, experimentally demonstrated for a metal–dielectric nanocrescent.³⁰ However, the quantitative predictability of these techniques still remains vague.

In this paper we demonstrate full 3D tomographic reconstruction of two coupled silver nanocuboids and measured EEL spectra and maps for a series of tilt angles. Instead of attempting a tomographic reconstruction of the plasmon fields (with exception of two interface modes to be discussed at the end), we used the precise 3D geometry of the particles as an input for EELS simulations^{14,31–33} and computed EEL spectra and maps for direct comparison with experiment. The rationale behind this approach is that (i) EEL maps contain a vast amount of (partly dependent) information,^{27,29} providing access to the entire plasmonic mode spectrum, and (ii) the predictability of EELS simulations has matured in recent years to the point where experiment and simulation can be compared on par. Our work renders plasmonic EELS capable for quantitative juxtaposition of

experiment and simulation and significantly improves on previous simulation approaches using idealized geometries, such as perfectly symmetric cylinders, triangles, or cuboids, which neglected imperfections of real nanostructures despite their possible impact on the nanoparticles' plasmonic properties.

We investigated pairs of 30 nm thick silver nanocuboids designed by electron beam lithography on a 15 nm thin Si_3N_4 membrane. To reduce charging during the experiment, the nanocuboids were coated with a thin layer ($\sim 1\text{--}2$ nm) of carbon (see [Supporting Information](#)). Among the various cube sizes and gap distances fabricated on the membrane, in this study we selected two cubes with a nominal edge length of 200 nm and a gap of 70 nm between the corners. This particle dimer sustains a large number of distinct plasmon modes, as further discussed below, and the gap size is small enough to allow coupling between the two cuboids.

EEL spectrum images and mass–thickness high-angle annular dark-field (HAADF) STEM images were acquired for 30 tilt angles between -67° and $+73^\circ$ (see [Supporting Information](#)). The measured EEL spectra were treated with a Richardson-Lucy deconvolution^{34,35} (see [Supporting Information](#)), and each resonance was integrated over 0.17 eV to generate 2D maps for comparison with simulation. The 3D morphology shown in [Figure 1](#) was derived from the HAADF signal with a total-variation (TV) minimization reconstruction algorithm.^{25,36} Our reconstruction scheme efficiently reduces missing wedge artifacts and recovers both top and bottom surfaces of the particles, which are impossible to obtain by conventional algorithms (see [Supporting Information](#)). While the bottom surface of the rhomboids, in contact with the substrate, are fairly flat, the upper side features significant roughness.

The reconstructed geometry of the silver cuboids served as an input for EELS simulations based on a boundary element method (BEM) approach and carried out with the MNPBEM toolbox.^{32,33} In the simulations we consider both the actual geometry of the sample and the Si_3N_4 substrate, and we use a

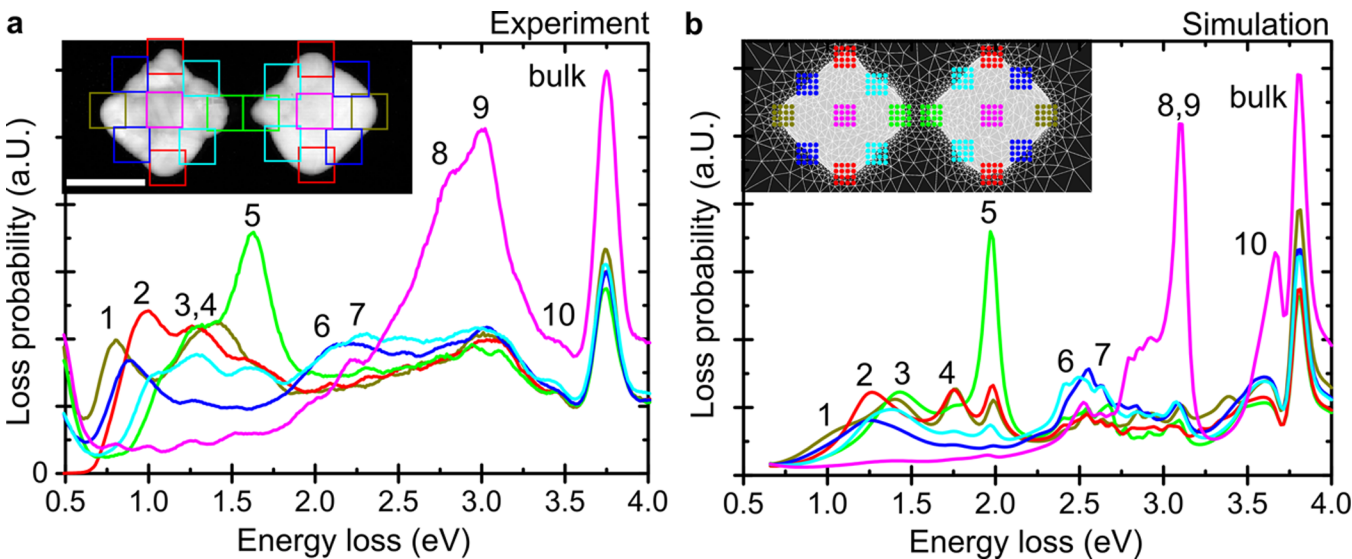


Figure 2. (a) Experimental and (b) simulated spectra extracted from different locations of the nanocuboids. For experimental data the spectra are averaged over regions marked by squares of the same color. For simulations spectra are averaged over the positions indicated by dots of the same color. In the spectra surface plasmon resonance peaks are labeled by numbers. Scale bars are 200 nm.

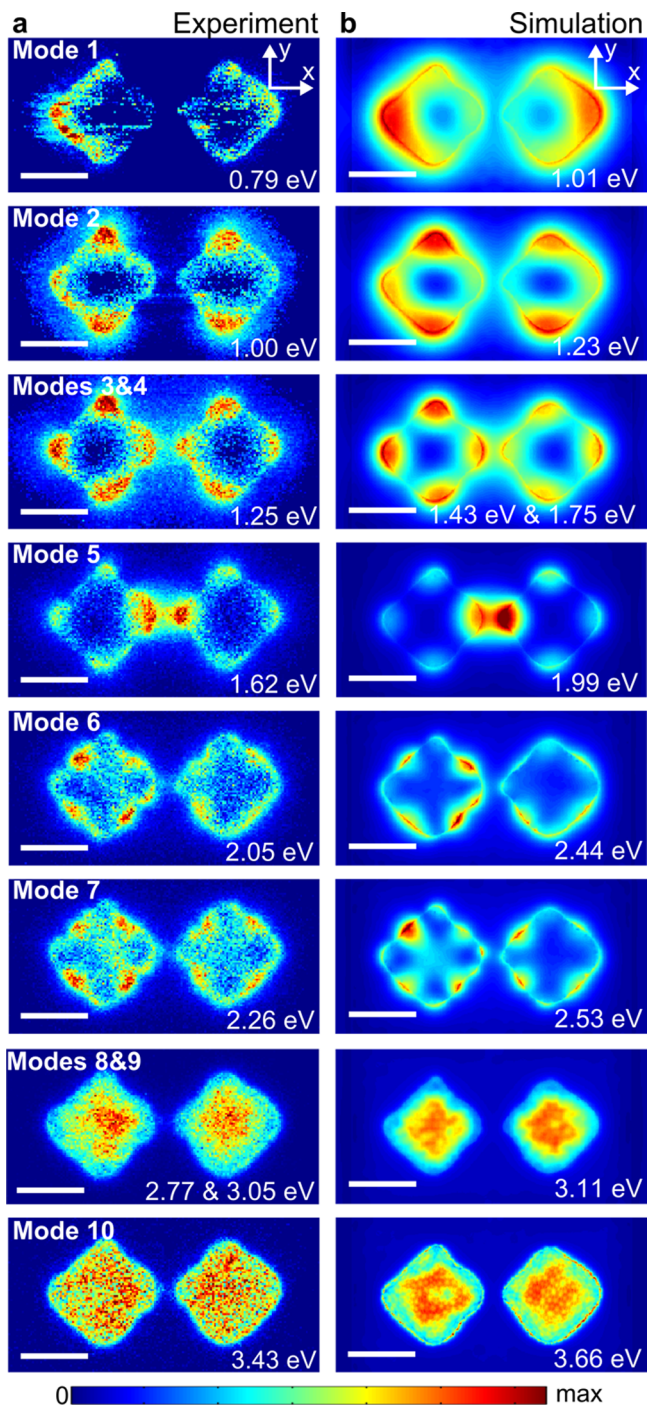


Figure 3. Surface plasmon resonance maps of the peaks indicated in Figure 2 extracted from experiments (a) and simulations (b). Modes 3 and 4 are overlapping in the experiment and summed for the simulations; modes 8 and 9 are overlapping in the simulation and summed for the experiment (see Supporting Information). The maximum in each map has been adapted for increased contrast, absolute peak intensities can be observed in the spectra in Figure 2. Scale bars are 200 nm.

tabulated dielectric function for silver extracted from optical data³⁷ (see Supporting Information).

Figure 2a and b shows EEL spectra from distinct spatial regions of the sample, extracted from experimental data and simulations, respectively. Experimental spectra were extracted from the spectrum image acquired at 0° tilt angle. Each

spectrum shows the averaged value obtained from the colored positions, which were chosen by symmetry arguments; averaging allowed us to improve the signal-to-noise ratio of experimental spectra. This averaging approach can be validated by comparing spectra from the individual positions (see Supporting Information). The following positions on the cuboids are compared: outer corners (dark yellow), inner corners (green), as well as upper and lower corners (red). The outer edges (dark blue), the inner edges (cyan), and the centers of the cuboids (magenta) are also displayed. We find excellent agreement between the experimental and simulated EEL spectra, with exception of a few systematic deviations to be discussed below. Multiple resonant modes can be identified, labeled 1–10, starting from the lowest energy. While modes 1–5 have their maxima at the corners of the cuboids, modes 6 and 7 have them at the edges, and modes 8–10 in the center of the cuboids.

The experimental EEL features are generally slightly broader than the simulated ones, which we attribute to the limited energy resolution of our experiments. Regarding the energetic positions of the modes, a slight mismatch between experiment and simulations is noticeable, with the experimental resonance energies typically occurring at lower values than the simulated ones. The origin of these shifts is investigated by extended simulations (see Supporting Information), and is most likely due to nanoparticle aging and the modification of grain sizes, which leads to a modification of the metal permittivity and in turn to a red-shift of the plasmonic resonances, in agreement to related studies.^{38,39} Supporting evidence for this interpretation is our observation of contrast changes for aged particles that went from a large crystal/polycrystalline state to near amorphization between deposition and analysis (see Supporting Information). In Figure 2, these shifts lead in the experimental spectra to an overlap of peaks 3 and 4 (separated peaks in simulations) and to a concurrence of peaks 8 and 9 (overlap in simulations).

At the plasmon peak energies, we extracted EEL maps from the experimental (Figure 3a, at 0° tilt angle) and simulation (Figure 3b) data. Modes 1–5 show maxima on the corners of the particles and are attributed to dipolar and quadrupolar modes based on their resonance energies and the spatial profile of the maps (see Supporting Information). Modes 1–3 show the spatial distribution of dipolar modes in the in-plane (*x*- and *y*-) directions. The dipole oriented along the *x*-direction splits up in energy into a bonding and antibonding mode, due to a coupling between the particles:⁴⁰ the bonding mode with dipolar moment in the *x*-direction (1) has the lowest energy, an uncoupled mode in the *y*-direction with dipolar moment (2) appears at a higher energy, and finally an antibonding dipolar mode in the *x*-direction has the highest energy (3). Because of an energetic overlap of modes 3 and 4 in the experiment, these modes are summed up for a more meaningful comparison in Figure 3 (see Supporting Information). Modes 4 and 5 are assigned to quadrupolar modes with the maxima on the corners of the particles. The coupling splits the quadrupoles into two distinct modes, a bonding (4) and an antibonding configuration (5).

In the range from 1.8 to 2.3 eV (2.2 to 2.7 eV) for the experiment (simulations), several other modes become apparent in Figure 2. Quadrupolar resonances, sensitive to the shape and the exact geometry of the particles, split up into several closely spaced signals as a result of structural imperfections. We exemplarily use modes 6 and 7 to highlight

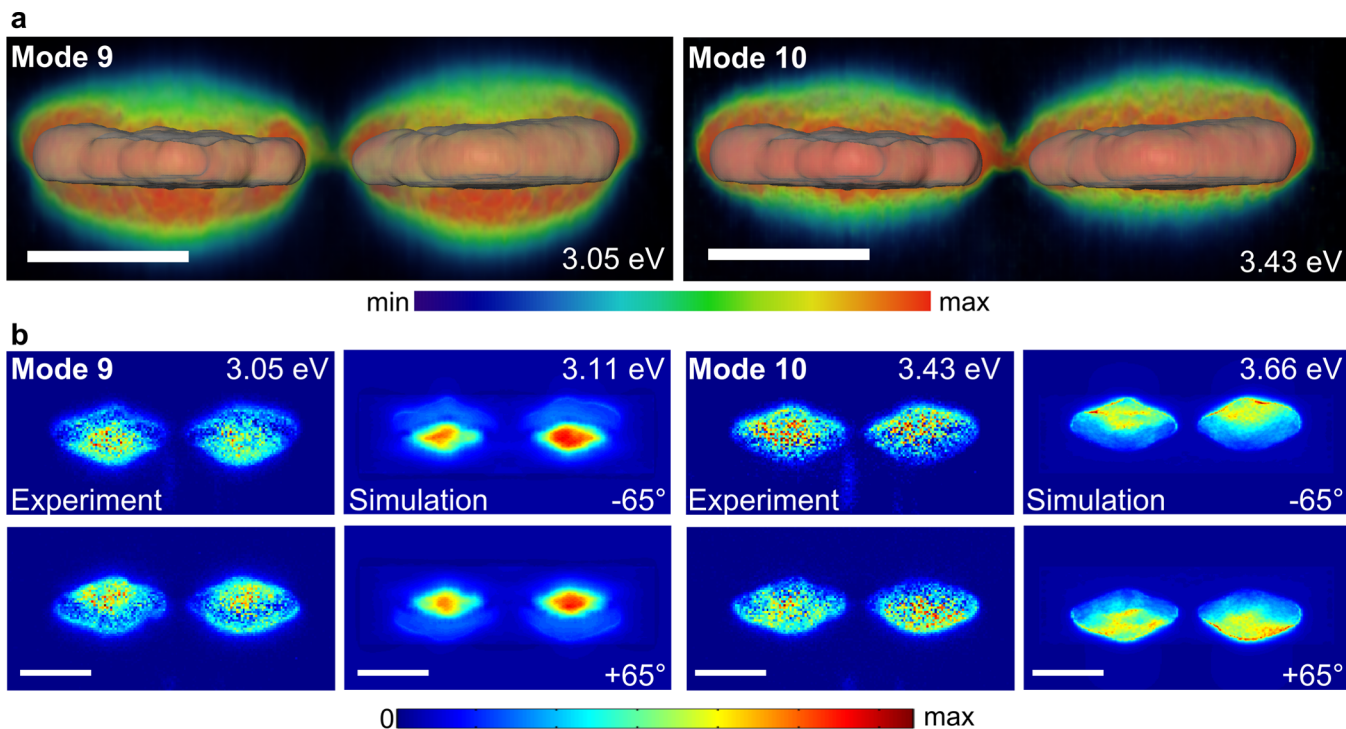


Figure 4. (a) 3D reconstructions of SiN/Ag interface mode (9) showing the maximum on the lower interface and Ag/C interface mode (10) showing the maximum on the upper interface. (b) Experimental and simulated maps of the same modes seen at tilt angles of -65° and $+65^\circ$. The maximum in each map has been adapted for increased contrast. Scale bars are 200 nm.

the high-quality correlation between the measured and simulated maps: For ideal nanoparticles these EEL maps would have maxima of equal strength at the edge centers; for the realistic geometry in Figure 2 we observe significant differences for the excitation at different edges and even two maxima on a single edge for mode 6. It is gratifying to see the one-to-one mapping of practically all features in the EEL maps, including the absence and presence of signals in the center region for modes 6 and 7, respectively.

At even higher energies, three additional resonances can be observed that are attributed to the breathing mode (8) and the surface plasmon interface modes between Ag and Si_3N_4 (9) and between Ag and carbon/vacuum (10), respectively. As the breathing mode shifts to lower energies, due to aging of silver, modes 8 and 9 can be discriminated from each other (see Supporting Information). By contrast, these modes overlap in the simulations and are summed up for comparison in Figure 3. Mode 10 is significantly weaker in comparison to the simulations (see Figure 2), probably due to damping caused by the carbon layer deposited on top of silver, an effect not accounted for in the simulations.

The question whether modes 9 and 10 stem from different interfaces is addressed by both a tomographic reconstruction and analysis of tilted EEL maps. Quite generally, the size of the structure is too large to allow a quasistatic reconstruction for all modes.^{27,28} However, for the vertical (z -) direction we expect the quasistatic reconstruction to provide a reasonable approximation (see Supporting Information). The map reconstructed from a tilt series of the respective EEL images is shown in Figure 4a. The lower energy mode (9) is indeed concentrated on the interface between silver and Si_3N_4 , while the higher energy mode (10) is located on the silver/carbon interface. The vertical distribution becomes apparent also when looking at EEL maps of modes 9 and 10 under large angular tilt

for both simulation and experimental data (Figure 4b) which are again in almost perfect agreement.

In conclusion, we have demonstrated how 3D reconstructed morphologies of metallic nanostructures can serve as an input for simulations of their plasmonic properties. Simulated EEL spectra and maps of coupled silver nanocuboids agree extremely well with experimental data, except for small deviations originating from incomplete information about the actual material composition and crystallinity. These differences could be eliminated if pure monocrystalline materials were used, or simulation tools would additionally consider the exact material properties. The 3D reconstruction of LSPR maps is feasible and allowed us to identify interface plasmons in the nanoparticles. Our work founds a basis for the detailed investigation of complex and realistic nanostructures, including geometry imperfections and surface roughness. It will be helpful for nanomaterial diagnostics but will also provide a tool for optimizing the material properties of complex nanostructures.

■ ASSOCIATED CONTENT

● Supporting Information

The Supporting Information is available free of charge on the ACS Publications website at DOI: [10.1021/acs.nanolett.5b03780](https://doi.org/10.1021/acs.nanolett.5b03780).

Methods including sample preparation, image acquisition, and data processing, plasmon resonance maps under several tilt angles, details about simulations, and considerations about sample aging (PDF)

■ AUTHOR INFORMATION

Corresponding Author

*E-mail: georg.haberfehlner@felmi-zfe.at.

Notes

The authors declare no competing financial interest.

ACKNOWLEDGMENTS

We thank Joachim Krenn and Harald Ditlbacher for access to and support with electron beam lithography and helpful discussion. This research has received funding from the European Union within the 7th Framework Program [FP7/2007-2013] under Grant Agreement no. 312483 (ESTEEM2). We acknowledge support by the Austrian Science Fund FWF under project P27299-N27, the SFB F49 NextLite, and NAWI Graz. Open-source software code has been used: The TV minimization solver TVAL3 (<http://www.caam.rice.edu/~optimization/L1/TVAL3/>) and the tomographic reconstruction toolbox ASTRA (<http://sourceforge.net/projects/astra-toolbox/>).

REFERENCES

- (1) Maier, S. A. *Plasmonics: Fundamentals and Applications*; Springer: Boston, MA, 2007.
- (2) Schuller, J. A.; Barnard, E. S.; Cai, W.; Jun, Y. C.; White, J. S.; Brongersma, M. L. *Nat. Mater.* **2010**, *9* (3), 193–204.
- (3) Anker, J. N.; Hall, W. P.; Lyandres, O.; Shah, N. C.; Zhao, J.; Van Duyne, R. P. *Nat. Mater.* **2008**, *7* (6), 442–453.
- (4) Batson, P. E. *Phys. Rev. Lett.* **1982**, *49* (13), 936–940.
- (5) Chu, M.-W.; Myroshnychenko, V.; Chen, C. H.; Deng, J.-P.; Mou, C.-Y.; García de Abajo, F. J. *Nano Lett.* **2009**, *9* (1), 399–404.
- (6) Rossouw, D.; Couillard, M.; Vickery, J.; Kumacheva, E.; Botton, G. A. *Nano Lett.* **2011**, *11* (4), 1499–1504.
- (7) Boudarham, G.; Feth, N.; Myroshnychenko, V.; Linden, S.; García de Abajo, J.; Wegener, M.; Kociak, M. *Phys. Rev. Lett.* **2010**, *105* (25), 255501.
- (8) Koh, A. L.; Fernández-Domínguez, A. I.; McComb, D. W.; Maier, S. A.; Yang, J. K. W. *Nano Lett.* **2011**, *11* (3), 1323–1330.
- (9) Duan, H.; Fernández-Domínguez, A. I.; Bosman, M.; Maier, S. A.; Yang, J. K. W. *Nano Lett.* **2012**, *12* (3), 1683–1689.
- (10) Schmidt, F.-P.; Ditlbacher, H.; Hohenester, U.; Hohenau, A.; Hofer, F.; Krenn, J. R. *Nano Lett.* **2012**, *12* (11), 5780–5783.
- (11) Schmidt, F. P.; Ditlbacher, H.; Hofer, F.; Krenn, J. R.; Hohenester, U. *Nano Lett.* **2014**, *14* (8), 4810–4815.
- (12) Bosman, M.; Keast, V. J.; Watanabe, M.; Maaroof, A. I.; Cortie, M. B. *Nanotechnology* **2007**, *18* (16), 165505.
- (13) Nelayah, J.; Kociak, M.; Stéphan, O.; García de Abajo, F. J.; Tencé, M.; Henrard, L.; Taverna, D.; Pastoriza-Santos, I.; Liz-Marzán, L. M.; Colliex, C. *Nat. Phys.* **2007**, *3* (5), 348–353.
- (14) García de Abajo, F. J. *Rev. Mod. Phys.* **2010**, *82* (1), 209–275.
- (15) Koh, A. L.; Bao, K.; Khan, I.; Smith, W. E.; Kothleitner, G.; Nordlander, P.; Maier, S. A.; McComb, D. W. *ACS Nano* **2009**, *3* (10), 3015–3022.
- (16) Kociak, M.; Stéphan, O. *Chem. Soc. Rev.* **2014**, *43* (11), 3865–3883.
- (17) Schaffer, B.; Hohenester, U.; Trügler, A.; Hofer, F. *Phys. Rev. B: Condens. Matter Mater. Phys.* **2009**, *79* (4), 041401.
- (18) N'Gom, M.; Li, S.; Schatz, G.; Erni, R.; Agarwal, A.; Kotov, N.; Norris, T. B. *Phys. Rev. B: Condens. Matter Mater. Phys.* **2009**, *80* (11), 113411.
- (19) Möbus, G.; Doole, R. C.; Inkson, B. J. *Ultramicroscopy* **2003**, *96* (3–4), 433–451.
- (20) Weyland, M.; Midgley, P. A. *Microsc. Microanal.* **2003**, *9* (6), 542–555.
- (21) Gass, M. H.; Koziol, K. K. K.; Windle, A. H.; Midgley, P. A. *Nano Lett.* **2006**, *6* (3), 376–379.
- (22) Midgley, P. A.; Dunin-Borkowski, R. E. *Nat. Mater.* **2009**, *8* (4), 271–280.
- (23) Yedra, L.; Eljarrat, A.; Arenal, R.; Pellicer, E.; Cabo, M.; López-Ortega, A.; Estrader, M.; Sort, J.; Baró, M. D.; Estradé, S.; Peiró, F. *Ultramicroscopy* **2012**, *122*, 12–18.
- (24) Haberfehlner, G.; Bayle-Guillemaud, P.; Audit, G.; Lafond, D.; Morel, P. H.; Jousseau, V.; Ernst, T.; Bleuet, P. *Appl. Phys. Lett.* **2012**, *101* (6), 063108.
- (25) Haberfehlner, G.; Orthacker, A.; Albu, M.; Li, J.; Kothleitner, G. *Nanoscale* **2014**, *6* (23), 14563–14569.
- (26) Midgley, P. A.; Thomas, J. M. *Angew. Chem., Int. Ed.* **2014**, *53* (33), 8614–8617.
- (27) Hörl, A.; Trügler, A.; Hohenester, U. *Phys. Rev. Lett.* **2013**, *111* (7), 076801.
- (28) Nicoletti, O.; de la Peña, F.; Leary, R. K.; Holland, D. J.; Ducati, C.; Midgley, P. A. *Nature* **2013**, *502* (7469), 80–84.
- (29) Hörl, A.; Trügler, A.; Hohenester, U. *ACS Photonics* **2015**, *2* (10), 1429–1435.
- (30) Atre, A. C.; Brenny, B. J. M.; Coenen, T.; García-Etxarri, A.; Polman, A.; Dionne, J. A. *Nat. Nanotechnol.* **2015**, *10* (5), 429–436.
- (31) Myroshnychenko, V.; Rodríguez-Fernández, J.; Pastoriza-Santos, I.; Funston, A. M.; Novo, C.; Mulvaney, P.; Liz-Marzán, L. M.; García de Abajo, F. J. *Chem. Soc. Rev.* **2008**, *37* (9), 1792–1805.
- (32) Hohenester, U.; Trügler, A. *Comput. Phys. Commun.* **2012**, *183* (2), 370–381.
- (33) Hohenester, U. *Comput. Phys. Commun.* **2014**, *185* (3), 1177–1187.
- (34) Gloter, A.; Douiri, A.; Tencé, M.; Colliex, C. *Ultramicroscopy* **2003**, *96* (3–4), 385–400.
- (35) Lazar, S.; Botton, G. A.; Zandbergen, H. W. *Ultramicroscopy* **2006**, *106* (11–12), 1091–1103.
- (36) Li, C.; Yin, W.; Jiang, H.; Zhang, Y. *Comput. Optim. Appl.* **2013**, *56* (3), 507–530.
- (37) Johnson, P. B.; Christy, R. W. *Phys. Rev. B* **1972**, *6* (12), 4370–4379.
- (38) Bosman, M.; Zhang, L.; Duan, H.; Tan, S. F.; Nijhuis, C. A.; Qiu, C.; Yang, J. K. W. *Sci. Rep.* **2014**, *4*, 5537.
- (39) Trügler, A.; Tinguely, J.-C.; Jakopic, G.; Hohenester, U.; Krenn, J. R.; Hohenau, A. *Phys. Rev. B: Condens. Matter Mater. Phys.* **2014**, *89* (16), 165409.
- (40) Hohenester, U.; Ditlbacher, H.; Krenn, J. R. *Phys. Rev. Lett.* **2009**, *103* (10), 106801.